

# Beaming, Baryon-Loading, and the Synchrotron Self-Compton Component in Gamma-Ray Burst Blast Waves Energized by External Shocks

Charles D. Dermer<sup>1</sup>, James Chiang<sup>2,1</sup>, & Kurt E. Mitman<sup>3,1</sup>

## ABSTRACT

We present detailed calculations of nonthermal synchrotron and synchrotron self-Compton (SSC) spectra radiated by blast waves that are energized by interactions with a uniform surrounding medium. Radio, optical, X-ray and gamma-ray light curves and spectral indices are calculated for a standard parameter set that yields hard GRB spectra during the prompt emission phase. Because no lateral spreading of the blast-wave is assumed, the calculated temporal breaks represent the sharpest breaks possible from collimated outflows in a uniform surrounding medium. Absence of SSC hardenings in observed GRB X-ray afterglows indicates magnetic field generation toward equipartition as the blast wave evolves. EGRET detections of 100 MeV–GeV photons observed promptly and 90 minutes after GRB 940217 are attributed to nonthermal synchrotron radiation and SSC emission from a decelerating blast wave, respectively. The SSC process will produce prompt TeV emission that could be observed from GRBs with redshifts  $z \lesssim 0.1$ , provided  $\gamma$ - $\gamma$  opacity in the source is small. Measurements of the time dependence of the 100 MeV–GeV spectral indices with the planned *GLAST* mission will chart the evolution of the SSC component and test the external shock scenario. Transient optical and X-ray emissions from misaligned GRBs are generally much weaker than on-axis emissions produced by dirty and clean fireballs that would themselves not trigger a GRB detector; thus detection of long wavelength transients not associated with GRBs will not unambiguously demonstrate GRB beaming.

## 1. Introduction

The discovery of X-ray afterglows and optical and radio counterparts to gamma-ray bursts (GRBs) has enabled redshift measurements of GRB sources and hosts, thereby confirming the hypothesis that GRBs are cosmologically distant and therefore very powerful (e.g., Costa et al. 1997; van Paradijs et al. 1997; Frail et al. 1998). The prompt gamma-ray emissions reach, as in the case of GRB 990123, directional energy releases  $\partial E/\partial\Omega$  as large as  $\sim 3 \times 10^{53}$  ergs sr<sup>-1</sup> (Kulkarni et al. 1999). The blast-wave model successfully accounts for the temporal power-law

---

<sup>1</sup>E. O. Hulburt Center for Space Research, Code 7653, Naval Research Laboratory, Washington, DC 20375-5352

<sup>2</sup>JILA, University of Colorado, Campus Box 440, Boulder, CO 80309-0440

<sup>3</sup>Thomas Jefferson High School for Science and Technology, 6560 Braddock Road, Alexandria, VA 22312

decays observed in many X-ray and optical afterglows which were predicted several years prior to their discovery (Paczynski & Rhoads 1993; Katz 1994; Mészáros & Rees 1997). In this model, a relativistic blast wave is energized as it passes through and captures material from an external medium. The power-law decay results mainly from this energizing process and the accompanying blast-wave deceleration (see, e.g., Vietri 1997; Waxman 1997; Wijers, Mészáros, & Rees 1997).

The degree of GRB blast-wave collimation is a crucial unknown. Breaks in the temporal indices of the afterglow emissions as a consequence of beaming are implied by analytic estimates (Rhoads 1997, 1999; Sari, Piran, & Halpern 1999; Panaitescu & Mészáros 1999; Wei & Lu 1999) and numerical calculations (Moderski, Sikora, & Bulik 1999). Temporal breaks have been observed in some GRB optical afterglows, namely GRB 990123 (Kulkarni et al. 1999) and GRB 990510 (Harrison et al. 1999), and have been used to argue for beaming. Beaming is important since knowledge of the degree of collimation is required to determine GRB source origins. Neither compact object coalescence scenarios nor collapsar/hypernova models invoking neutrino annihilation or magnetohydrodynamic processes make sufficient fireball energy to account for the largest measured GRB energies without invoking opening half-angles  $\psi \lesssim 10^\circ$  (e.g., Janka et al. 1999; Popham, Woosley, & Fryer 1999).

A second crucial question related to the origin of GRBs is whether the prompt emission results from collisions between a succession of shells ejected from the GRB engine (Rees & Mészáros 1994; Kobayashi, Piran, & Sari 1997) or is instead due to interactions of a single impulsive relativistic blast wave with inhomogeneities in the external medium (Mészáros & Rees 1993; Dermer & Mitman 1999). If a ring of material is formed in stellar collapse events, then extended GRB ejection events could result, although greater total energy releases occur for shorter accretion episodes (Popham et al. 1999). Detailed calculations of coalescence events indicate that the maximum energy output occurs over time scales of milliseconds (Ruffert & Janka 1999). Thus if it is established that the GRB engine ejects plasma over an extended period of several seconds to tens of seconds, a collapsar/hypernova scenario would seem to be favored. In contrast, an impulsive, highly beamed event in a low-density ( $n_0 \lesssim 1 \text{ cm}^{-3}$ ) surrounding environment would point to compact object merger events as the origin of GRBs, because a massive star progenitor to a collapsar event is probably accompanied by strong stellar winds and a high-density ( $n_0 \gg 100 \text{ cm}^{-3}$ ) surrounding medium.

In this paper, we present calculations of prompt GRB emissions and afterglows involving a single impulsive ejection event in the framework of the external shock model. Although both colliding shell (Daigne & Mochkovitz 1998) and external shock (Panaitescu & Mészáros 1998; Dermer, Böttcher, & Chiang 1999) models can reproduce the generic spectral behavior of GRB pulses and profiles, only the external shock model has been shown (Böttcher & Dermer 1999) to quantitatively fit the  $\gtrsim 1 \text{ s } t_{50}$  duration distribution and the distribution of the peaks  $E_{\text{pk}}$  of the  $\nu F_\nu$  spectra of GRBs measured with BATSE (Mallozzi et al. 1995). Fits to these distributions require a wide range of  $\partial E/\partial\Omega$  values and initial Lorentz factors  $\Gamma_0$ . This is not in conflict with relativistic beaming scenarios and the finding that the values of  $E_{\text{pk}}$  are preferentially measured

within the triggering range of BATSE, because BATSE is most likely to trigger on emissions from GRB blast waves with  $E_{\text{pk}}$  within its observing energy range (Dermer et al. 1999). Fireballs with a wide range of baryon-loading parameters are thereby implied. Hence the external shock model predicts new classes of dirty and clean fireballs that have not been detected due to design limitations of space-based X-ray and gamma-ray telescopes (Dermer, Chiang, & Böttcher 1999). As shown here, the dirty fireballs can produce transients that could be mistaken for the delayed emissions from off-axis GRBs.

Prompt and afterglow behaviors from beamed GRBs are studied by choosing parameters derived from the external shock model that yield hard spectra in the prompt gamma-ray emitting phase. In Section 2, we describe our numerical treatment and choice for a standard parameter set with  $\Gamma_0 = 300$ . We present detailed calculations of the afterglow light curves from radio through TeV energies in Section 3 for a jet with  $\psi = 10^\circ$ , and show calculations of the spectral and temporal index variations due to beaming. Predictions for gamma-ray temporal and spectral variation in the prompt and early afterglow phases due to the evolution of the SSC component in an external shock model are presented in Section 4. The external shock model predicts spectral aging of the SSC component in the early afterglow, leading to a soft-to-hard evolution in the GeV spectra in the early afterglow phase. Light curves at a range of observing angles for blast waves with  $\Gamma_0 = 100$  and 1000 are presented in Section 5, where properties of long-wavelength transients due to dirty fireballs and misaligned GRB outflows are compared and contrasted. We summarize in Section 6.

## 2. GRB Blast-Wave Calculations

The calculations are based on the code described in the paper by Chiang & Dermer (1999), and the model employs the standard blast-wave physics assumptions (see, e.g., Wijers, Mészáros, & Rees 1997; Panaitescu & Mészáros 1998; Sari, Piran, & Narayan 1998 and references therein). The blast wave is modeled by a relativistically expanding surface that subtends a constant solid angle fraction  $f = \delta\Omega/4\pi$  of the full sky. The blast wave has initial bulk Lorentz factor  $\Gamma_0$  and total directional fireball energy  $\partial E/\partial\Omega = 10^{54}E_{54}$  ergs/( $4\pi$  sr). We choose  $E_{54} = 1$  for the calculations in this paper. Although a more complicated geometry that accounts for lateral expansion of the shell (see Rhoads 1999) can be easily implemented, the constant solid angle assumption produces the sharpest breaks in the light curves (Moderski et al. 1999). Sharper temporal breaks could be produced if  $f$  decreases with distance  $x$  from the explosion site, but we consider this prospect unlikely since the pressure of the external medium would not exceed the jet pressure until the blast wave decelerates to nonrelativistic speeds. The surrounding external medium is assumed to be uniform with density  $n_0 = 100 \text{ cm}^{-3}$ . This density is intermediate to values ranging from  $10^{-3} \lesssim n_0 \lesssim 10^6 \text{ cm}^{-3}$  that are considered in most GRB models.

As the blast wave sweeps up material from the external medium, it is assumed that a constant fraction  $\epsilon_e$  of the swept-up kinetic energy of the particles is converted to the internal energy of nonthermal electrons, and that the electrons are injected with a power-law distribution with index

$p$  between minimum and maximum electron Lorentz factors  $\gamma_{\min}$  and  $\gamma_{\max}$ , respectively. The value of  $\gamma_{\min}$  is obtained by numerically solving the expression

$$\left(\frac{p-1}{p-2}\right) \frac{\gamma_{\min}^{2-p} - \gamma_{\max}^{2-p}}{\gamma_{\min}^{1-p} - \gamma_{\max}^{1-p}} = 1 + \epsilon_e \frac{m_p}{m_e} (\Gamma - 1), \quad (1)$$

which follows from kinetic-energy and number conservation for the swept-up particles, assuming prompt acceleration and no particle escape. In order to maximize radiative efficiencies, we assume that the injected energy is equally shared between the protons and electrons and let  $\epsilon_e = 0.5$ . The value of  $\gamma_{\max} = \epsilon_{\max}(3e/\sigma_T B)^{1/2} = 4.6 \times 10^7 \epsilon_{\max} B^{-1/2}(\text{G})$  of the injected electrons is given with respect to the limit on  $\gamma_{\max}$  that is obtained by balancing the synchrotron loss time scale with the time scale for an electron to execute a Larmor orbit (Guilbert, Fabian, & Rees 1983; de Jager & Baring 1997), where  $B$  is the magnetic field intensity. Eq. (1) has no solution if  $\epsilon_e$  is too large and  $\gamma_{\max}$  is too small, because this prescription may require that more energy than  $m_e c^2 (\gamma_{\max} - 1)$  must be given to each electron. We choose  $\epsilon_{\max} = 1.0$  in our calculations.

The nonthermal electrons lose energy by synchrotron, SSC, and adiabatic energy-loss processes, as described by Chiang & Dermer (1999). The angle-averaged synchrotron emissivity function of Crusius & Schlickeiser (1986) is used to compute the synchrotron emissivity, and Jones' (1968) expression for the Compton emissivity spectrum in the head-on approximation is used to calculate the SSC component (see also Blumenthal & Gould 1970). The value of  $B$  is determined according to the standard equipartition prescription

$$\frac{B^2}{8\pi} = \epsilon_B \lambda n_0 m_p c^2 (\Gamma^2 - \Gamma), \quad (2)$$

where we let the compression ratio  $\lambda = 4$  in our calculations. Blast-wave evolution is self-consistently followed from momentum conservation by calculating the change in internal energy due to the added energy of swept-up particles, taking into account energy losses of the nonthermal electrons. Although electrons lose energy through adiabatic processes that could be rechanneled into the kinetic energy of the outflowing blast-wave fluid, we do not follow this flow of energy. The synchrotron self-absorption coefficient is calculated according to the standard radiation formulas as described by Dermer, Böttcher, & Chiang (1999, in preparation), and radiation spectra with angle-dependent effects of self-absorption are calculated and summed to produce the observed spectra and light curves measured at observing time  $t$  and photon energy  $E$ .

The absorption coefficient  $\kappa_{\gamma\gamma}(E')$  to photon-photon pair production attenuation at comoving frame photon energy  $E'$  is calculated from the formulas of Gould & Schröder (1965) and Brown, Mikaelian, & Gould (1973). The emergent spectra are reduced by the factor  $[1 - \exp(-\tau_{\gamma\gamma})]/\tau_{\gamma\gamma}$ , where  $\tau_{\gamma\gamma}(E') = \kappa_{\gamma\gamma}(E') \Delta x / \cos \xi$ ,  $\Delta x$  is the comoving frame shell width, and  $\xi$  is the angle between the normal to the element of radiating surface and the observer. We let  $\Delta x = x/\Gamma$  (Blandford & McKee 1976; Panaitescu & Mészáros 1998). The reinjection of the pairs and the subsequent cascade are not followed in this calculation, but the net reduction of radiated power by the inclusion of this process is found to be a small ( $\lesssim 10\%$ ) fraction of the total radiant power for the parameters

studied here. The received spectra are calculated by summing over all elements of the radiating surface that contribute to emission observed at time  $t$ .

The values we choose for our standard set of parameters are motivated by observations of GRB emission during the prompt phase. For example, as shown by Chiang & Dermer (1999), this means that the magnetic field equipartition parameter should be  $\epsilon_B \lesssim 10^{-4}$  during the prompt emission phase in order to avoid forming cooling distributions which have photon fluxes  $\Phi(E) \propto E^{-3/2}$  below the peak photon energy,  $E_{\text{pk}}$ . Such soft spectra are not commonly observed in GRBs (see Preece et al. 1998; Cohen et al. 1997). We note, however, that in order to fit the spectral and temporal behavior of the *afterglow* emission, we require the electron injection power-law index to be  $p \simeq 2.5$  (see, e.g., Wijers & Galama 1999). In accordance with the standard blast wave model, we also assume that  $\epsilon_B$  and the other microphysical parameters  $p$ ,  $\epsilon_e$ , and  $\epsilon_{\text{max}}$  do not change with time. This is obviously an oversimplification, and could strongly affect afterglow evolution and the importance of the SSC component in the afterglow phase. In fact our results suggest that  $\epsilon_B$  increases toward equipartition as the blast wave evolves with time, as explained below.

Figure 1 shows results for our standard parameter set with  $\Gamma_0 = 300$ ,  $E_{54} = 1$ ,  $n_0 = 100 \text{ cm}^{-3}$ ,  $p = 2.5$ ,  $\epsilon_e = 0.5$ ,  $\epsilon_{\text{max}} = 1.0$ , and  $\epsilon_B = 10^{-4}$ . Here we show results for an uncollimated blast wave. The deceleration radius and time scale for these parameters are  $x_{\text{dec}} = (3E_0/4\pi n_0 m_p c^2 \Gamma_0^2)^{1/3} = 2.6 \times 10^{16} \text{ cm}$  and  $t_{\text{dec}} = x_{\text{dec}}/2\Gamma_0^2 c = 9.6 \text{ s}$ , respectively. The heavy solid curve in Fig. 1a shows the dependence of  $\Gamma$  on distance  $x$  from the explosion center. This evolutionary behavior was obtained by an iterative procedure to ensure self-consistency, and has clearly converged. Because we assume that  $\epsilon_B$  is independent of time and is assigned such a small value, the GRB spectral properties are in the weak cooling regime throughout its evolution (Sari et al. 1998). Even so, the blast-wave does not follow an adiabatic evolutionary behavior with  $\Gamma(x) \propto x^{-3/2}$ , but rather a  $\Gamma(x) \propto x^{-1.9}$  behavior in the asymptotic regime  $1 \ll x/x_{\text{dec}} \ll \Gamma_0^{1/2}$ . Although the lowest energy nonthermal electrons do not efficiently cool, much of the energy carried by the higher energy nonthermal electrons is efficiently radiated away, causing the blast-wave dynamics to depart considerably from adiabatic behavior.

Fig. 1b shows the temporal evolution of the comoving electron energy spectra  $N(\gamma)$  multiplied by  $\gamma^2$ , where  $\gamma$  is the electron Lorentz factor in the comoving blast wave frame. Fig. 1c shows the calculated  $\nu L_\nu$  photon spectra. The various curves in Figs. 1b and 1c range from 0.01 s to  $10^8$  s in factors of 10, with the later curves showing progressively lower energy breaks. The lower-energy synchrotron and higher-energy SSC components in the  $\nu L_\nu$  spectra of Fig. 1c are evident, and the SSC component dominates the energy losses of the electrons in much of the afterglow phase for this set of parameters. SSC processes can be important when  $\epsilon_e/\lambda\epsilon_B \gtrsim 1$  (see Sari, Narayan, & Piran 1996; Moderski et al. 1999 for a more precise criterion). For the parameters in Fig. 1,  $\epsilon_e/\lambda\epsilon_B \cong 10^3$ , and the SSC component dominates electron cooling, particularly in the afterglow phase when the Klein-Nishina effects are less important for electron Compton scattering. At very late times  $t \gg 10^7$  s, however, the synchrotron component again dominates when most of the higher energy electrons have cooled to give a very soft electron spectrum.

Light curves at radio, optical, X-ray, soft gamma-ray, GeV, and TeV photon energies are shown in Fig. 1d in an  $L_\nu$  representation. A number of interesting effects are apparent here. The emission at soft gamma-ray energies rises and decays on the deceleration time scale due to the energization of the blast wave and the subsequent deceleration. The peaking of the TeV light curve due to SSC radiation mirrors the behavior of the synchrotron peak in the 100 keV light curve. The optical and X-ray light curves show delayed emission compared to the soft gamma-ray light curve. This is due to the time required for the  $\nu F_\nu$  peak of the synchrotron emission, arising from the lowest-energy cooled electrons in the electron distribution function, to pass into the various observing ranges as the blast wave decelerates. The delayed peaking of the lower energy synchrotron emission represents a prediction of the external shock model (Dermer et al. 1999). As the blast-wave continues to decelerate, the self-Compton radiation produces time-dependent flattenings of the light curves at successively later times for the progressively lower GeV, 100 keV, X-ray, and optical frequencies. The softenings of the light curves at  $t \gtrsim 5 \times 10^7$  s occurs when the blast wave reaches nonrelativistic speeds.

The X-ray and optical emissions display temporal behaviors  $\propto t^{-1.75}$  at  $t \sim 10^3$ – $10^4$  s and  $\propto t^{-1.4}$ , at  $t \sim 10^5$ – $10^7$  s. A hardening of the temporal behavior of the X-ray emission occurs at  $t \gtrsim 3 \times 10^4$  s due to the onset of the SSC component, and begins to decay more rapidly at  $\gg 10^6$  s, when the peak of the SSC component has passed through the X-ray regime. Typical observed temporal indices at X-ray and optical frequencies of GRBs are somewhat flatter than these values; this would result if a smaller value of  $\epsilon_e$  were used in the simulation, yielding a blast wave evolution more nearly adiabatic, or if a harder electron index  $p$  were used. Lack of evidence for a delayed hardening from the SSC component in X-ray afterglow light curves suggests that the magnetic field strength increases towards  $\epsilon_B \sim 1$  in the afterglow phase (see Section 4.1). These calculations show that excess emission could be present in optical afterglow light curves at late times due to the appearance of the SSC component. Excess emission has been observed from GRB 970228 (Reichart 1999) and GRB 980326 (Bloom et al. 1999)  $\sim 10$ – $40$  days after the bursts and has been attributed to light from a supernova. This excess emission is very red and supports the interpretation of a supernova origin. To the extent that SSC hardenings have not been observed in X-ray afterglows, it seems less likely that such SSC hardenings would be detected in the optical light curves, even taking into account that optical telescopes have much better  $\nu F_\nu$  sensitivities than X-ray telescopes. Although a full parameter study has not been made, caution must be taken to assure that the Compton component from the blast wave does not introduce delayed excess emission in optical light curves. We do note, however, that depending on the physical parameters, excess emission in the late afterglow from SSC processes may be bluer at the outset than the synchrotron emission immediately preceding it and would make a transition over time to a redder spectrum. This is clearly seen in the X-ray spectral index shown in Fig. 4a. This behavior could then serve as a means of distinguishing it from supernova emission.

### 3. Blast-Wave Calculations of Beamed GRBs

Figures 2a and 2b show angle-dependent light curves at various frequencies for the same parameter set used in Fig. 1, except now we consider a jet with an opening half-angle of  $\psi = 10^\circ$ . For a one-sided jet, this angle represents 0.76% of the full sky. Light curves are evaluated at inclination angles  $\theta = 0^\circ, 10^\circ, 12^\circ, 15^\circ, 30^\circ, 60^\circ$ , and  $90^\circ$ . A temporal break due to beaming occurs in the  $\theta = 0^\circ$  curves at  $t \sim 10^5$  seconds, independent of energy, though the break is hidden at MeV and X-ray energies due to the emergence of the SSC component. The temporal break occurs when the angle  $\theta \sim \Gamma^{-1}$  of the Doppler beaming cone equals the jet opening angle  $\psi$ . For a blast-wave decelerating according to the approximation  $\Gamma(x) = \Gamma_0$  for  $x < x_{\text{dec}}$ , and  $\Gamma(x) = \Gamma_0(x/x_{\text{dec}})^{-g}$  for  $x > x_{\text{dec}}$ , the time  $t_b$  at which the temporal break is observed with respect to the time of the explosion is given by  $t_b \approx (1+z)[-x \cos \psi + \int_0^x dx' \beta^{-1}(x)']/c$ . Here  $c\beta(x) = c[1 - \Gamma(x)^{-2}]^{1/2}$  is the speed of the blast wave. This gives

$$\frac{ct_b}{(1+z)} = x_{\text{dec}} \left[ (\Gamma_0 \psi)^{1/g} (1 - \cos \psi) + \frac{2g + (\Gamma_0 \psi)^{2+1/g}}{2(2g+1)\Gamma_0^2} \right]. \quad (3)$$

Eq. (3) implies that the temporal break occurs at  $t_b \approx 10^5$  s for  $g \cong 1.9$ , in agreement with the numerical results.

Figure 2a shows 8.6 GHz radio, V-band, and 3 keV X-ray light curves calculated at the values of  $\theta$  listed above. The light curves at  $\theta < \psi$  are very similar, as can be seen by comparing the  $0^\circ$  and  $10^\circ$  curves, but the X-ray and optical light curves drop markedly in intensity once the observer is outside the beaming cone. The emission remains at a very low level until the Doppler cone of the beamed emission intersects the observer’s line of sight. Following the arguments given to derive eq. (3), we find that an off-axis observer ( $\theta > \psi$ ) starts to detect emission at a level comparable to an on-axis observer at times given by eq. (3), but with  $\psi$  replaced by  $\theta - \psi$ .

Figure 2b shows light curves calculated at 4.8 GHz radio, MeV, GeV, and TeV photon energies for the same parameters as used in Fig. 2a. No intervening absorption of the GeV or TeV fluxes are shown in this figure; for cosmologically distant GRB sources the absorption of TeV photons due to interactions with the cosmic diffuse infrared radiation field would significantly reduce the flux compared with the intrinsic emission, depending sensitively on the redshift of the source (see, e.g., Salamon & Stecker 1998). The effects of intrinsic  $\gamma$ - $\gamma$  attenuation are important for the TeV light curves, though not for the GeV and lower energy light curves, and have been taken into account as previously described. In order to illustrate the energy dependence of this attenuation, we plot in Fig. 3 the optical depth to  $\gamma$ - $\gamma$  attenuation as a function of observed photon energy along radial lines-of-sight from the explosion center through the blast-wave shell. Each of the optical depth curves corresponds to a spectrum shown in Fig. 1c. As in Fig. 1c, the vertical lines indicate the energies of the various light curves we plot in Fig. 1d. It is evident from this figure that this source of optical depth is only significant for  $\gtrsim 100$  GeV–TeV energies (long-dashed line).

One of the most notable features of Fig. 2b is the appearance of extended GeV emission compared to the times of the peaks of the MeV and TeV fluxes. For the parameters used here, the

GeV band is situated between the peaks of the synchrotron and SSC fluxes, and the GeV emission is formed from synchrotron emission of the highest energy electrons in the prompt phase, and primarily from the SSC process in the early afterglow phase (compare Fig. 1c). The delayed emission in the GeV band arises from the same effect that causes the predicted energy-dependent delays in the peaks of the synchrotron emission at photon energies  $E_\gamma \ll E_{\text{pk}}$ , as described analytically by Dermer et al. (1999).

An effect (see also Dermer 1999) revealed in the calculations shown in Figs. 2a and 2b is that the ratios of the on-axis to off-axis fluxes are much larger at higher photon energies. Hence the  $\gamma$ -ray and X-ray synchrotron fluxes for on-axis observers are very bright in comparison with the fluxes that would be detected for an identical source that is directed away from the observer. This ratio is smaller at optical frequencies, and the fluxes are comparable for on-axis and misaligned sources at radio frequencies where the emission persists at comparable levels for about the same length of time. This suggests that radio surveys to monitor misaligned GRB sources would not have to scan over the same region more than once per day to once per week in order to catch transient misaligned GRBs. In the case of optical emission, this time scale is  $\sim$  once per hour or so. The appearance of prompt optical emission in GRB 990123 (Akerlof et al. 1999) demonstrates, however, that an additional prompt optical component, due possibly to emission from the reverse shock (Mészáros & Rees 1993a; Sari & Piran 1999) which has not been included in this calculation, could produce brighter and more rapidly varying long wavelength transients.

Spectral and temporal indices are plotted in Figs. 4a and 4b, respectively, for the radio, optical, and hard X-ray light curves from Figs. 1 and 2a. Here we write the flux density  $F_\nu(\nu, t) \propto \nu^{-\alpha} t^{-\chi}$  at frequency  $\nu$ . The heavy curves show the  $\theta = 0^\circ$  case with  $\psi = 10^\circ$ , and the light curves show the uncollimated case. The radio, optical, and X-ray spectral indices are calculated between 4.8 and 8.6 GHz, the V and I bands, and 3 and 100 keV, respectively. At early times  $t \ll t_{\text{dec}}$ , the indices all approach  $\alpha = -1/3$ , corresponding to the  $F_\nu \propto \nu^{1/3}$  behavior of the elementary synchrotron emissivity spectrum from an electron distribution function with a low-energy cutoff  $\gamma_{\text{min}} \gg 1$ . Only at later times after the comoving electron density increases does the radio emission become self-absorbed to form a spectrum rising roughly as  $F_\nu \propto \nu^{-2}$ . In the early afterglow phase  $1 \ll t/t_{\text{dec}} \ll 10^3$ , the optical and X-ray spectral indices soften but never distinctly display an index characteristic of an uncooled distribution which, for  $p = 5/2$ , is  $\alpha_{\text{uncooled}} = (p - 1)/2 = 0.75$ . For the chosen parameters, cooling is important for all but the lowest energy injected electrons.

In the afterglow phase  $10^3 \ll t/t_{\text{dec}} \ll 10^6$ , the optical spectral indices approaches the value expected for a cooled electron distribution, namely  $\alpha_{\text{cooled}} = p/2 = 1.25$ . The X-ray index never reaches this asymptote because the X-ray spectrum hardens as the SSC component starts to become important in this band at  $t \gtrsim 10^4$  s. The optical spectral index reaches the cooling spectral index asymptote at  $t \gtrsim 3 \times 10^4$  s. Beaming effects on the spectral indices begin to be important at  $t \gtrsim 10^5$  s.

The temporal indices shown in Fig. 4b change in concert with the spectral indices of Fig. 4a.



The radio emission, with its inverted spectrum, rises monotonically in flux following the prompt phase, and the temporal index remains negative (i.e., increasing flux) until late times  $t \approx 10^7$  s for the case with no collimation. In contrast, collimation softens the radio temporal index by about 0.5 units (Rhoads 1999; Sari, Piran, & Halpern 1999). The optical R-band temporal index is  $\approx 0$  in the early afterglow phase due to competition between Doppler deceleration and the increasing number of nonthermal electrons injected through the sweep-up process. The optical temporal index in the uncollimated case approaches the value  $\chi \sim 1.4$  at  $t \gtrsim 3 \times 10^4$  s. For the beamed case, the optical light curve decays much more rapidly when  $t \gtrsim 10^5$  s. This is also the case for the X-ray decay, though the appearance of the SSC component complicates the behavior by introducing a hardening and a slower decay. This also occurs in the optical spectrum, though at late times  $t \gtrsim 10^6$  s.

#### 4. Gamma Ray Light Curves

Fig. 5 shows the MeV, GeV, and TeV gamma-ray light curves of Fig. 2b multiplied by time. Plotted in this way, the curves indicate the period during which a gamma-ray telescope with negligible background will detect most of its counts. As in the previous section, the heavy and light curves refer to the beamed and uncollimated cases, respectively. The pronounced softening of the light curves at  $t \gtrsim 10^5$  s due to beaming is apparent.

##### 4.1. Hardenings in MeV and X-ray Light Curves during the Early Afterglow

The MeV light curves show strong emission that peaks on the deceleration time scale — this is, of course, the GRB itself. A hardening due to the onset of the SSC component occurs at  $t \approx 10^3$  s and reaches a secondary maximum at  $t \approx 10^5$  s. The maximum MeV flux from the SSC component is 4–5 orders of magnitude less than the peak flux measured in the prompt phase of the GRB (see Figs. 1 and 2a), but the longer duration available to accumulate signal will partially compensate if the background is sufficiently low.

Unfortunately, strong and variable backgrounds at hard X-ray and soft gamma-ray energies over time scales from hours to days make it unlikely that an SSC hardening in the MeV afterglow could be observed with BATSE on the *Compton Observatory*. A very strong GRB with a signal to noise ratio  $\gtrsim 10^3$  could make it possible to observe the SSC hardening with a pointed instrument. The OSSE instrument on *Compton* has a program to slew toward GRBs. Persistent emission decaying as a power-law has been detected as late as  $\sim 10^3$  s after a GRB trigger in two cases, namely GRB 970827 and GRB 97110 (Matz et al. 1999). No evidence of hardening in the light curve was observed at later times, but the S/N ratio may not have been sufficiently great for detection of delayed emission from these GRBs.

The lack of distinct SSC hardenings has not been observed in X-ray afterglows of BeppoSax, which our calculations indicate would begin at  $\sim (3 \times 10^4 - 10^5) \times (1 + z)$  s after the GRB.

Even though the X-ray afterglow flare occurring  $\sim 1\text{--}3$  days after GRB 970508 shows a correlated spectral hardening and temporal flattening (Piro et al. 1998), we do not think that this is due to the SSC component because the flaring behavior is more abrupt than expected from our calculations. The flare is more likely due to enhanced emission radiated by the blast wave when it encounters a density enhancement in the circumburst medium. The simplest explanation that no distinct SSC component has been observed in X-ray afterglows is that  $\epsilon_B$  increases from the very low value found during the prompt phase. Consequently the relative importance of the SSC component would decrease with time. Depending on the time scale over which the magnetic field increases, a hardening in the MeV component might therefore be still more difficult to detect than indicated by Fig. 5.

#### 4.2. GeV Afterglows and the Case of GRB 940217

In contrast with the MeV light curves, the prospect of detecting delayed GeV emission from the SSC component is more favorable because of the much smaller backgrounds at GeV energies and the earlier onset of the SSC hardening. The photon fluxes are, however, much smaller at GeV energies than at MeV energies, so a GeV detector will detect many fewer GRBs than an MeV telescope with comparable effective area. Specifically, the EGRET instrument on *Compton* has detected 7 GRBs above 30 MeV (Catelli, Dingus, & Schneid 1998). EGRET has about the same effective area as the Large Area Detectors on BATSE, but views only 1/20th of the full sky as compared with 40% for BATSE. This indicates that EGRET detects only  $\sim 3\%$  of the BATSE bursts that fell within its field of view, consistent with the much smaller photon fluxes at 100 MeV and GeV energies compared with the 50–300 keV fluxes measured with BATSE.

The GeV light curve in Fig. 5 shows two peaks. The early maximum coincident with the MeV peak is the high-energy extension of the synchrotron component, and the second maximum peaking at  $\approx 5000$  s is due primarily to SSC radiation. The dimmer synchrotron flux at GeV energies compared to MeV energies, coupled with the longer interval over which the relatively brighter SSC signal can be accumulated, make it more probable that delayed GeV emission rather than MeV emission can be detected from a GRB, provided of course, that a sufficiently bright GRB should be observed by a GeV detector.

We propose that the high-energy emission observed 90 minutes after GRB 940217 (Hurley et al. 1994) was in consequence of the SSC component becoming increasingly dominant at later times as the deceleration of the blast wave caused the SSC emission to sweep through the GeV band. This explanation also accounts for the appearance of the extraordinary 18 GeV photon observed with EGRET 90 minutes after the onset of the GRB, rather than during the prompt phase. The GeV band resides in the  $\nu F_\nu$  valley between the synchrotron and SSC components. During the prompt phase, the flux of 1–10 GeV photons is very low and the spectrum is very soft; furthermore there is not much time to accumulate signal. The emergence of the SSC component in this band as the blast wave decelerates maintains the 1–10 GeV flux level at a roughly constant value (see

Fig. 1c) over an extended period of time which, with its harder spectrum, can favor the detection of the highest energy emission during the early afterglow phase rather than during the prompt phase.

The planned *Gamma ray Large Area Space Telescope (GLAST)* mission<sup>1</sup> will have larger effective area and field-of-view than EGRET, so will likely be able to monitor the evolution of the SSC spectral feature due to blast wave deceleration. The time dependence of the MeV–GeV and GeV–TeV spectral behavior is plotted in the inset to Fig. 5. During the prompt phase, the MeV–GeV photon spectral index from the cooled synchrotron radiation is  $\sim 2.25$ , in accordance with measurements of  $> 30$  MeV EGRET spectra (Catelli et al. 1998). The GeV–TeV index is much harder because it is primarily sampling the harder SSC component. As the blast wave begins to decelerate in earnest during the early afterglow phase, the MeV–GeV index hardens as the SSC radiation sweeps into this waveband. We would then expect that the GeV–TeV index approaches the  $\alpha = 5/4$  cooling spectrum, but the effects of  $\gamma$ - $\gamma$  attenuation on the TeV emission produces an additional softening. The MeV–GeV index does approach the cooled synchrotron limit at late times until the blast wave reaches the nonrelativistic regime. Spectral hardening in the MeV–GeV band in the early afterglow phase due to the deceleration of the blast wave as it interacts with a smooth external medium constitutes generic behavior of the external shock model which can be tested with *GLAST*.

### 4.3. TeV Emission from GRBs

Figure 5 also shows that TeV photons from the SSC process during the prompt phase of a GRB is roughly coincident in time with the prompt MeV synchrotron emission. For this set of parameters, the  $\nu F_\nu$  flux is somewhat dimmer at TeV energies than at MeV energies. Even though this calculation suggests that strong TeV flux should be emitted from most GRBs, it would only be detected from nearby, low redshift bursts for which the attenuation due to intergalactic infrared emission is small (provided that the intrinsic  $\gamma$ - $\gamma$  attenuation in the source is also small). According to the calculations of Stecker & de Jager (1998), the optical depth to TeV photons is  $\cong 0.5$ -1 at  $z = 0.075$ , and increases strongly with increasing redshift. Thus we should expect TeV emission to be detected only rarely from a GRB.

Searches for TeV emission from GRBs using the water Cherenkov Milagrito detector have been recently reported (McEnery et al. 1999). By looking for excesses in the  $t_{90}$  time intervals of 54 BATSE GRBs, enhanced emission associated with TeV radiation was reported from one candidate, GRB 970417a. The chance probability for detecting such an excess was calculated to be less than the  $1.5 \times 10^{-3}$ . Our calculations are consistent with detection of TeV emission from GRBs that are close enough to avoid strong attenuation from the diffuse radiation field.

---

<sup>1</sup><http://glast.gsfc.nasa.gov/SRD>

## 5. Baryon-Loading Effects in Beamed GRBs

Up to this point, we have examined multiwavelength light curves for beamed and uncollimated outflows employing a standard parameter set that is consistent with typical durations, spectra, and energy fluxes observed from GRBs during their prompt phase. As demonstrated in the studies by Dermer et al. (1999) and Böttcher & Dermer (1999) where a simplified analytic form for emission from blast waves was employed, the spectral properties of GRBs in the prompt phase are rather insensitive to  $n_0$  and  $E_0$  — varying typically as the cube root of these quantities — but are very strongly dependent on  $\Gamma_0$  and a parameter related to the magnetic field. We have already described how the magnetic field equipartition parameter  $\epsilon_B$  must be assigned a value much smaller than unity to be compatible with spectral properties of GRBs during the prompt phase; this may, in fact, indicate the difficulties of strong field generation during the early episodes of the blast wave. There is no *a priori* reason to suppose, however, that  $\Gamma_0$  must be assigned a value of 300.

In Figs. 6 and 7 we present calculations for  $\Gamma_0 = 100$  and  $\Gamma_0 = 1000$ , respectively, with all other parameters, including  $\psi$ , the same as in the previous sections. The main differences between the light curves with different baryon loading are due to the strong  $\Gamma_0$ -dependences of  $t_{\text{dec}}$  and the maximum  $\nu L_\nu$  peak flux  $\Phi_{\text{pk}}$ , which is measured at photon energy  $E_{\text{pk}}$ , the peak of the  $\nu L_\nu$  spectrum in the prompt phase. In accordance with analytical results,  $t_{\text{dec}} \propto \Gamma_0^{-8/3}$  (Rees & Mészáros 1992) and  $\Phi_{\text{pk}} \propto \Gamma_0^{8/3}$  (Dermer et al. 1999). Thus dirty fireballs with small values of  $\Gamma_0$  are extended and reach smaller peak  $\nu F_\nu$  fluxes at lower values of  $E_{\text{pk}}$ , whereas the clean fireballs with large values of  $\Gamma_0$  produce brief, intense episodes of emission having larger peak  $\nu F_\nu$  fluxes at higher values of  $E_{\text{pk}}$ .

For the dirty ( $\Gamma_0 = 100$ ) and clean ( $\Gamma_0 = 1000$ ) fireball cases in Figs. 6b and 7b, the MeV flux maxima occur at  $t \approx 63$  s and  $t \approx 0.25$  s and reach maximum flux values of  $2 \times 10^{49}$  ergs  $\text{s}^{-1}$  and  $10^{52}$  ergs  $\text{s}^{-1}$ , respectively. The MeV flux maximum for the standard case in Fig. 2b in Fig. 7b occurs at  $t \approx 4$  s and  $1.5 \times 10^{51}$  ergs  $\text{s}^{-1}$ . The product of the peak flux and the time of flux maximum, which corresponds roughly to the duration of the GRB, is proportional to the number of counts that would be measured by a GRB detector; these products for the dirty, standard, and clean cases are  $\sim 10^{51}$ ,  $6 \times 10^{51}$ , and  $3 \times 10^{51}$  ergs, respectively. Triggering biases in an MeV detector therefore strongly favor detection of the standard case over the dirty fireball due to its lower flux and more extended duration. Such biases also favor the detection of the standard case over the clean fireball case, though the level of background in determining relative detectability of clean fireballs is more important here than for dirty fireballs. These detailed calculations support the analysis of (Dermer et al. 1999) and Böttcher & Dermer (1999) that the origin of the peaking  $\nu F_\nu$  distribution observed with BATSE is due to selection biases in GRB detectors and the spectral properties of relativistic blast waves.

By directly overlaying Figs. 2a, 6a, and 7a, it is clear that X-ray emissions from dirty fireballs which do not trigger a GRB detector are generally much brighter than the X-ray emissions from misaligned GRBs with  $\theta \gg \psi$ . Thus we argue that any detection of so-called “orphan” afterglows

(see Rhoads 1999) will more likely be due to dirty fireballs than off-axis GRBs.

Figure 8 illustrates the preceding points more clearly by plotting 100 keV light curves for the standard, dirty and clean fireball cases. This photon energy corresponds to the typical energy of photons detected by BATSE within its triggering range (for a low redshift GRB). A GRB detector will more likely be triggered by a blast wave which places the peak of its  $\nu F_\nu$  flux in the triggering range of the detector. The strong detector biases against detecting a long duration dirty fireball, which reaches a relatively very low maximum flux value at 100 keV compared to the case with  $\Gamma_0 = 300$ , are clearly displayed by the inset.

According to this analysis, burst detectors that trigger in a particular energy range are more sensitive to GRBs with  $E_{\text{pk}}$  in the energy range of the detector. We therefore predict that the planned *Swift* mission, with its Burst Alert Telescope<sup>2</sup> that triggers in the 50-150 keV range, would detect a sample of GRBs with, on average, longer durations and lower  $E_{\text{pk}}$  fluxes than those observed with BATSE.

## 6. Summary

Because of its fewer underlying assumptions and success in explaining GRB phenomenology during the prompt gamma-ray emission phase, we have restricted calculations in this paper to the external shock model. Our calculations follow blast waves that are energized and decelerate by sweeping up material from a uniform surrounding medium, and we employ parameters consistent with typical durations, spectra, and  $E_{\text{pk}}$  values measured from BATSE GRBs. We have examined the effects of blast-wave collimation on the light curves. Although we do not consider lateral expansion of the blast wave, as recently examined numerically by Moderski et al. (1999), our calculations improve upon this study by including SSC processes and a self-consistent treatment of blast-wave dynamics.

Our beaming calculations reproduce effects pointed out in the earlier analytic and numerical studies, namely that afterglows decay more rapidly for beamed than for uncollimated outflows. When the SSC component is unimportant, the spectrum also softens as beaming effects on the temporal decay become important. Collimated GRB outflows directed away from an observer will produce extended transients at X-ray and optical frequencies at a flux level orders of magnitude less than transients observed along the jet axis. The relative flux levels of on-axis and misaligned jet sources at radio infrared and radio frequencies are much smaller than at optical and X-ray frequencies. Transients from misaligned GRB outflows could be confused with on-axis clean and dirty fireball bursts, so detection of such long wavelength transients will not unambiguously demonstrate beaming.

---

<sup>2</sup><http://swift.gsfc.nasa.gov/instruments/bat.html>

The calculations of the SSC component demonstrate a number of potentially observable effects:

1. Hardenings of the multiwavelength light curves appear as the SSC component sweeps through successively lower observing frequencies at increasingly later times. For the standard parameter set used here, TeV emission is due to SSC radiation in the prompt GRB phase, and the onset of SSC hardenings at GeV, MeV, X-ray, and optical frequencies occurs at  $\sim 200$ ,  $3 \times 10^3$ ,  $10^5$ , and  $3 \times 10^6$  s, respectively.
2. Because distinct SSC hardenings have not been observed in GRB X-ray afterglows, we argue that the magnetic field in the blast wave increases toward its equipartition value as the blast wave evolves. A stronger magnetic field has the effect of reducing the importance of the SSC component. If this interpretation is correct, then the SSC hardenings would not be expected in late time optical afterglows, strengthening the likelihood that observed hardenings are due either to an underlying host galaxy or supernova emission.
3. We attribute the prompt and delayed 100 MeV–GeV emissions observed from GRB 940217 with EGRET (Hurley et al. 1994) primarily to nonthermal synchrotron and SSC emission, respectively. The external shock model predicts a soft-to-hard evolution of the spectrum at GeV energies in the early afterglow phase that could be tested with the planned *GLAST* experiment. Taking into account internal pair production attenuation, we find that TeV SSC emission at  $\nu F_\nu$  levels comparable that of the prompt MeV synchrotron radiation could be observed from nearby GRBs with  $z \lesssim 0.1$ , where attenuation by the cosmic diffuse infrared radiation field is small.

Our summary result of this study is that SSC emission produces a broad spectral feature that can be used for the study of processes in GRB blast waves. When analyzed with correlated X-ray and soft gamma-ray observations, observations of the SSC component might make it also possible to infer magnetic field strengths and Doppler factors, as has been done in analyses of relativistic outflows in blazars (e.g., Catanese et al. 1997). Because the SSC radiation is most intense during the prompt and early afterglow phases, the GeV range is an especially important regime for GRB studies because the deceleration of the blast wave — or the acceleration of a radiating surface due to collisions between internal shocks — can be charted by monitoring spectral and temporal evolution in this band.

This work is supported through the NASA Astrophysical Theory Program (DPR S-13756G) and the Office of Naval Research.

## REFERENCES

Akerlof, C., et al. 1999, *Nature*, 398, 400

- Blandford, R. D., & McKee, C. F. 1976, *Phys. Fluids*, 19,1130
- Bloom, J. S., et al. 1999, *Nature*, in press (astro-ph/9905301)
- Blumenthal, G. R., & Gould, R. J. 1970, *RMP*, 42, 237
- Böttcher, M., & Dermer, C. D. 1999, *ApJ*, in press (astro-ph/9812059)
- Brown, R. W., Mikaelian, K. O., & Gould, R. J. 1973, *Astrophysical Letters*, 14, 203
- Catanese, M. et al. 1997, *ApJ*, 487, L143
- Catelli, J. R., Dingus, B. L., & Schneid, E. J. 1998, in *Gamma-Ray Bursts, 4th Huntsville Symposium*, eds. C. A. Meegan, R. D. Preece, & T. M. Koshut (AIP: New York), 309
- Chiang, J., & Dermer, C. D. 1999, *ApJ*, 512, 699
- Cohen, E., Katz, J. I., Piran, T., Sari, R., Preece, R. D., & Band, D. L. 1997, *ApJ*, 488, 330
- Costa, E., et al. 1997, *Nature*, 387, 783
- Crusius, A., & Schlickeiser, R. 1986, *A&A*, 164, 16
- Daigne, F., & Mochkovitz, R. 1999, *MNRAS*, 296, 275
- de Jager, O. C., & Baring, M. G. 1997, in *Proceedings of the Fourth Compton Symposium*, ed. C. D. Dermer, M. S. Strickman, & J. D. Kurfess (AIP: New York), p. 171
- Dermer, C. D. 1999, *Astroparticle Physics*, 11, 1
- Dermer, C. D., & Mitman, K. E. 1998, *ApJ*, 513, L5
- Dermer, C. D., Böttcher, M., & Chiang, J. 1999, *ApJ*, 515, L49
- Dermer, C. D., Chiang, J., & Böttcher, M. 1999, *ApJ*, 513, 656
- Frail, D. A., Kulkarni, S. R., Nicastro, L., Feroci, M., & Taylor, G. B. 1998, *Nature*, 389, 261
- Gould, R. J., & Schröder, G. P. 1965, *Phys. Rev.*, 155, 1404
- Guilbert, P. W., Fabian, A. C., & Rees, M. J. 1983, *MNRAS*, 205, 593
- Harrison, F. A., et al. 1999, *ApJ*, 523, L121
- Hurley, K. C., et al. 1994, *Nature*, 372, 652
- Janka, H.-T., Eberl, T., Ruffert, M., & Fryer, C. L. 1999, *ApJ*, submitted (astro-ph/9908290)
- Jones, F. C. 1968, *Phys. Rev.*, 167, 1159
- Katz, J. I. 1994, *ApJ*, 422, 248
- Kobayashi, S., Piran, T., & Sari, R. 1999, *ApJ*, 513, 679
- Kulkarni, S. R., et al. 1999, *Nature*, 398, 389
- Mallozzi, R. S. et al. 1995, *ApJ*, 454, 597
- Matz, S. M., Share, G. H., Grove, J. E., & Johnson, W. N. 1999, in preparation

- McEnery, J. et al. 1999, report at GeV–TeV Gamma Ray Astrophysics Workshop, Snowbird, Utah, August 13-16, 1999
- Mészáros, P., & Rees, M. J. 1993, *ApJ*, 405, 278
- Mészáros, P., & Rees, M. J. 1993a, *ApJ*, 418, L59
- Mészáros, P., & Rees, M. J. 1997, *ApJ*, 476, 232
- Moderski, R., Sikora, M., & Bulik, T. 1999, *ApJ*, in press (astro-ph/9904310)
- Panaitescu, A., & Mészáros, P. 1998, *ApJ*, 492, 683
- Paczyński, B., & Rhoads, J. 1993, *ApJ*, 418, L5
- Piro, L., et al. 1998, *A&A*, 331, L41
- Popham, R., Woosley, S. E., & Fryer, C. 1999, *ApJ*, 518, 356
- Preece, R. D., Briggs, M. S., Mallozzi, R. S., Pendleton, G. N., Paciesas, W. S., & Band, D. L. 1998, *ApJ*, 506, 23
- Rees, M. J., & Mészáros, P., 1992, *MNRAS*, 258, 41P
- Rees, M. J., & Mészáros, P., 1994, *ApJ*, 430, L93
- Reichart, D. E. 1999, *ApJ*, 521, L111
- Rhoads, J. E. 1997, *ApJ*, 487, L1
- Rhoads, J. E. 1999, *ApJ*, in press (astro-ph/9903399)
- Ruffert, M., & Janka, H.-T. 1999, *A&A*, 344, 573
- Salamon, M. H., & Stecker, F. W. 1998, *ApJ*, 493, 547
- Sari, R., Narayan, R., & Piran, T. 1996, 473, 204
- Sari, R., Piran, T., & Narayan, R. 1998, *ApJ*, 497, L17
- Sari, R., & Piran, T. 1999, *ApJ*, 520, 641
- Sari, R., Piran, T., & Halpern, J. P. 1999, *ApJ*, 519, L17
- Stecker, F. W., & de Jager, O. C. 1998, *A&A*, 334, L85
- van Paradijs, J., et al. 1997, *Nature*, 386, 686
- Vietri, M. 1997, *ApJ*, 478, L9
- Waxman, E. 1997, *ApJ*, 485, L5
- Wei, D. M., & Lu, T. 1999, astro-ph/9908273
- Wijers, R. A. M. J., Mészáros, P., & Rees, M. J. 1997, *MNRAS*, 288, L51
- Wijers, R. A. M. J., & Galama, T. J. 1999, *ApJ*, 523, 177



### Figure Captions

Fig. 1.— Numerical simulation using standard parameter set (see text). (a) Evolution of blast-wave Lorentz factor. Vertical dotted lines refer to observer times with respect to the time of explosion in factors of 10, with the left-most line at  $t = 1$  s. (b) Comoving electron energy distribution  $dN(\gamma;t)/d\gamma$  multiplied by  $\gamma^2$  for observer times ranging from  $t = 10^{-2}$  s to  $t = 10^8$  s in factors of 10. (c) Photon spectra in a  $E^2 dN/dtdE$  (or  $\nu L_\nu$ ) representation for observer times ranging from  $t = 10^{-2}$  s to  $t = 10^8$  s in factors of 10. (d) Light curves in an  $L_\nu$  representation at 8.6 GHz radio (solid curve), optical R band (dotted), 3 keV X-ray (dashed), 100 keV soft gamma-ray (dash-dotted), GeV (dashed/triple-dotted), and TeV (long-dashed) photon energies.

Fig. 2.— Light curves calculated at various observing energies and inclination angles  $\theta$  for a GRB with a standard parameter set and opening half-angle  $\psi = 10^\circ$  of the jet. The initial blast wave Lorentz factor  $\Gamma_0 = 300$ . Calculations of  $\theta = 0^\circ, 10^\circ, 12^\circ, 15^\circ, 30^\circ, 60^\circ$ , and  $90^\circ$  are shown, with the brighter peak fluxes reached by curves progressively closer to the jet axis. (a) Light curves at 8.6 GHz radio (solid curves), V-band optical (dotted), and 3 keV X-ray (dashed) are plotted. (b) Light curves at 4.8 GHz radio (solid curves), MeV (dot-dashed), GeV (dotted), and TeV (dashed) are plotted.

Fig. 3.— Optical depth to  $\gamma$ - $\gamma$  attenuation as a function of observed photon energy. The curves shown here correspond to the various spectra in Fig. 1c. Each curve is labeled at the left by  $\log_{10}(t_{\text{obs}})$ . The vertical lines indicate the energies of the light curves shown in Fig. 1d. For the standard set of parameters, photon-photon attenuation is clearly only important for the emission at energies  $\gtrsim 1$  TeV

Fig. 4.— Energy spectral indices and temporal indices for the uncollimated (light curves; from Fig. 1) and beamed (heavy curves; from Fig. 2) cases with  $\psi = 10^\circ$  and  $\theta = 0^\circ$ . (a) Energy spectral indices  $\alpha$  calculated between 4.8 and 8.6 GHz, the I and V bands, and 3 and 100 keV. (b) Temporal indices  $\chi$  calculated at 8.6 GHz, the R band, and 3 keV.

Fig. 5.— Product of  $\nu L_\nu$  flux and observing time  $t$  for the MeV, GeV, and TeV light curves using the  $\theta = 0^\circ$  case in Fig. 2b. Inset shows temporal variation of the broadband MeV–GeV and GeV–TeV energy spectral indices.

Fig. 6.— Same as Fig. 2, but for an initial blast wave Lorentz factor  $\Gamma_0 = 100$ .

Fig. 7.— Same as Fig. 2, but for an initial blast wave Lorentz factor  $\Gamma_0 = 1000$ .

Fig. 8.— Prompt and early afterglow 100 keV light curves for blast wave Lorentz factors  $\Gamma_0 = 1000$  (solid curve), 300 (dashed), and 100 (dotted). Inset shows light curves on a linear scale.

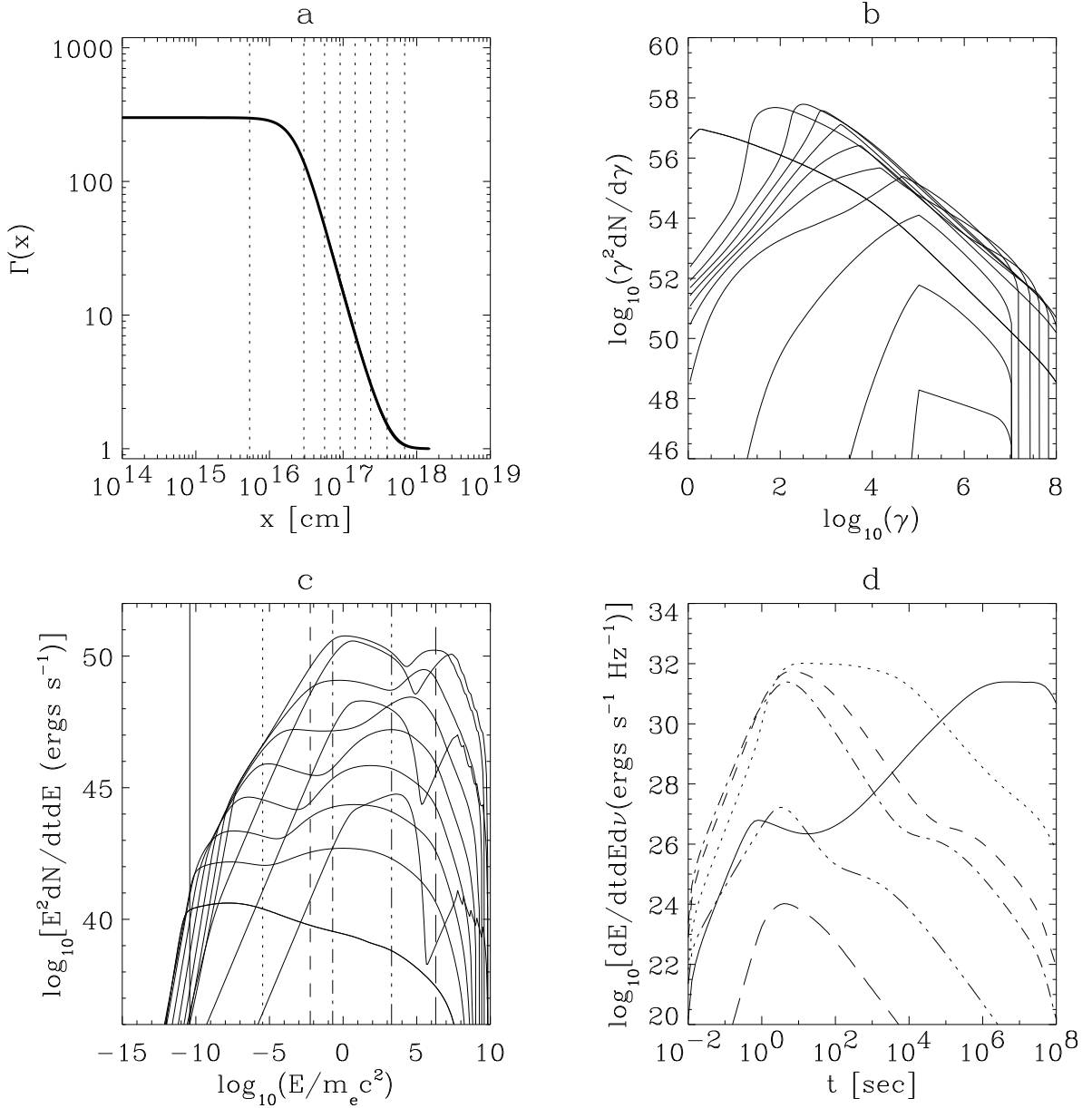


Fig. 1.— Numerical simulation using standard parameter set (see text). (a) Evolution of blast-wave Lorentz factor. Vertical dotted lines refer to observer times with respect to the time of explosion in factors of 10, with the left-most line at  $t = 1$  s. (b) Comoving electron energy distribution  $dN(\gamma; t)/d\gamma$  multiplied by  $\gamma^2$  for observer times ranging from  $t = 10^{-2}$  s to  $t = 10^8$  s in factors of 10. (c) Photon spectra in a  $E^2 dN/dt dE$  (or  $\nu L_\nu$ ) representation for observer times ranging from  $t = 10^{-2}$  s to  $t = 10^8$  s in factors of 10. (d) Light curves in an  $L_\nu$  representation at 8.6 GHz radio (solid curve), optical R band (dotted), 3 keV X-ray (dashed), 100 keV soft gamma-ray (dash-dotted), GeV (dashed/triple-dotted), and TeV (long-dashed) photon energies.

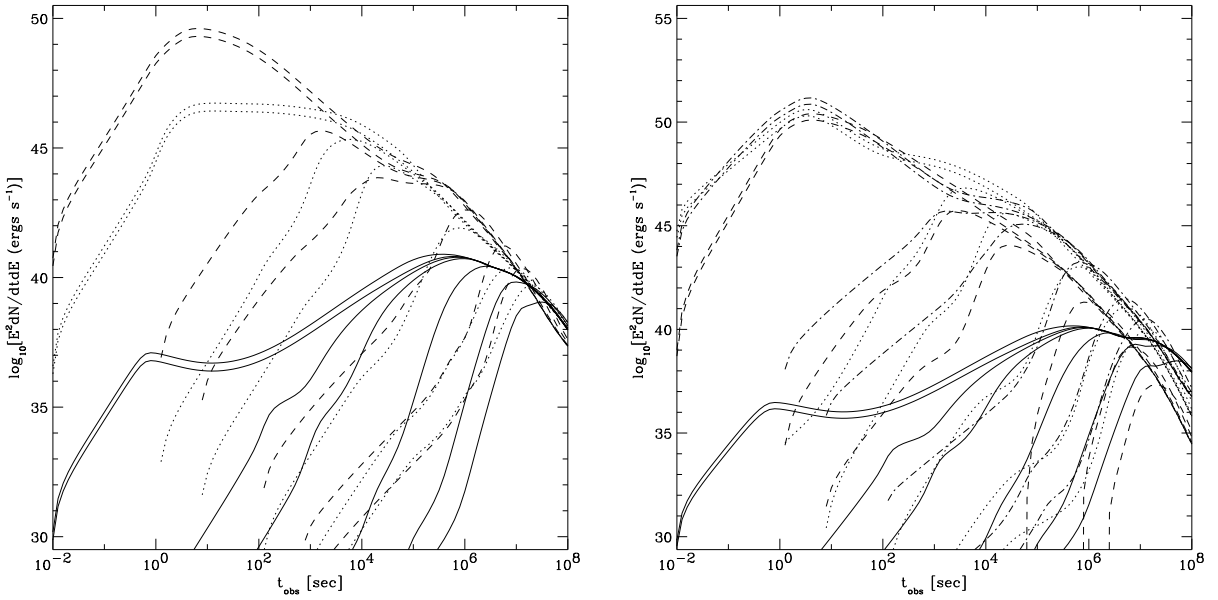


Fig. 2.— Light curves calculated at various observing energies and inclination angles  $\theta$  for a GRB with a standard parameter set and opening half-angle  $\psi = 10^\circ$  of the jet. The initial blast wave Lorentz factor  $\Gamma_0 = 300$ . Calculations of  $\theta = 0^\circ, 10^\circ, 12^\circ, 15^\circ, 30^\circ, 60^\circ$ , and  $90^\circ$  are shown, with the brighter peak fluxes reached by curves progressively closer to the jet axis. (a) Light curves at 8.6 GHz radio (solid curves), V-band optical (dotted), and 3 keV X-ray (dashed) are plotted. (b) Light curves at 4.8 GHz radio (solid curves), MeV (dot-dashed), GeV (dotted), and TeV (dashed) are plotted.

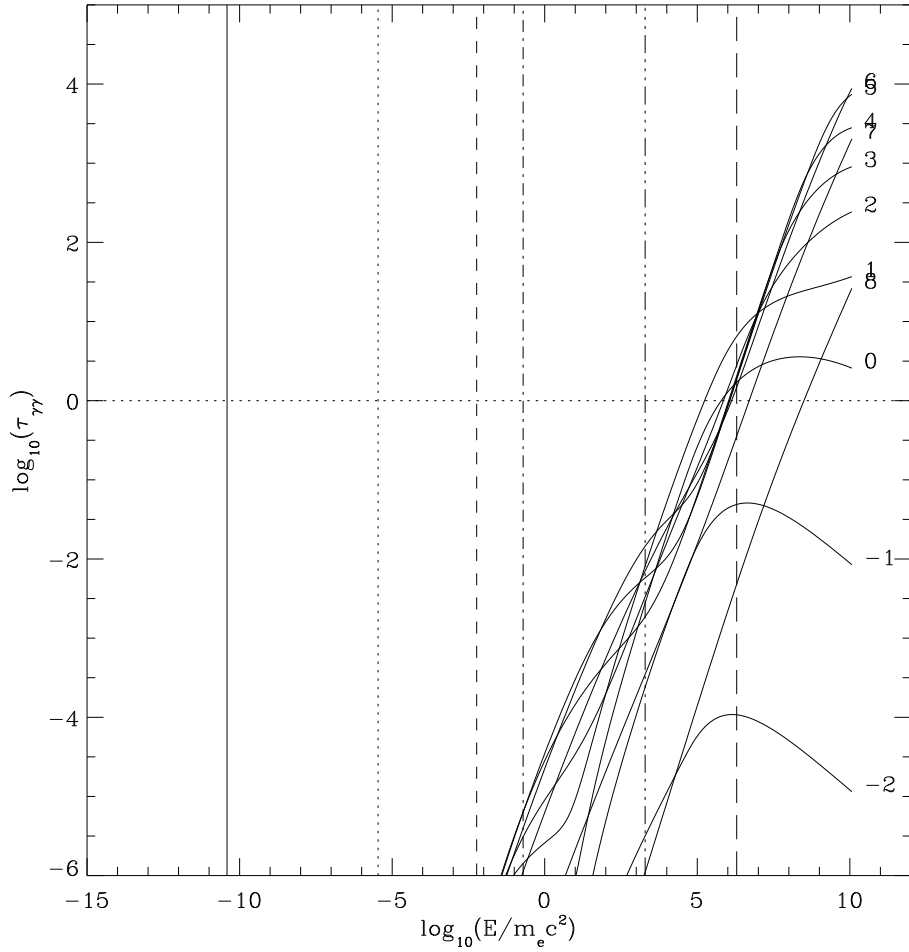


Fig. 3.— Optical depth to  $\gamma$ - $\gamma$  attenuation as a function of observed photon energy. The curves shown here correspond to the various spectra in Fig. 1c. Each curve is labeled at the left by  $\log_{10}(t_{\text{obs}})$ . The vertical lines indicate the energies of the light curves shown in Fig. 1d. For the standard set of parameters, photon-photon attenuation is clearly only important for the emission at energies  $\gtrsim 1$  TeV.

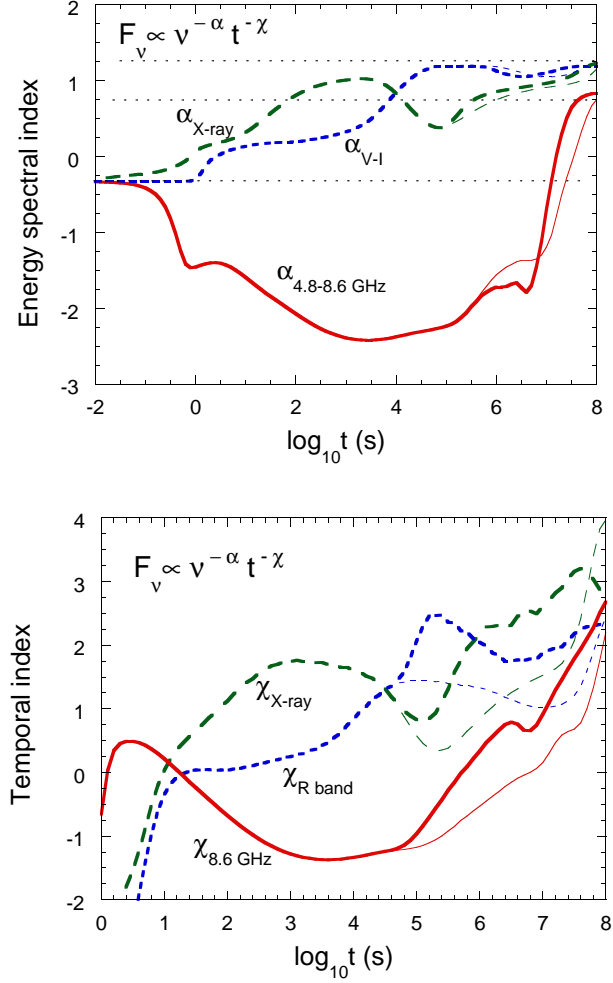


Fig. 4.— Energy spectral indices and temporal indices for the uncollimated (light curves; from Fig. 1) and beamed (heavy curves; from Fig. 2) cases with  $\psi = 10^\circ$  and  $\theta = 0^\circ$ . (a) Energy spectral indices  $\alpha$  calculated between 4.8 and 8.6 GHz, the I and V bands, and 3 and 100 keV. (b) Temporal indices  $\chi$  calculated at 8.6 GHz, the R band, and 3 keV.

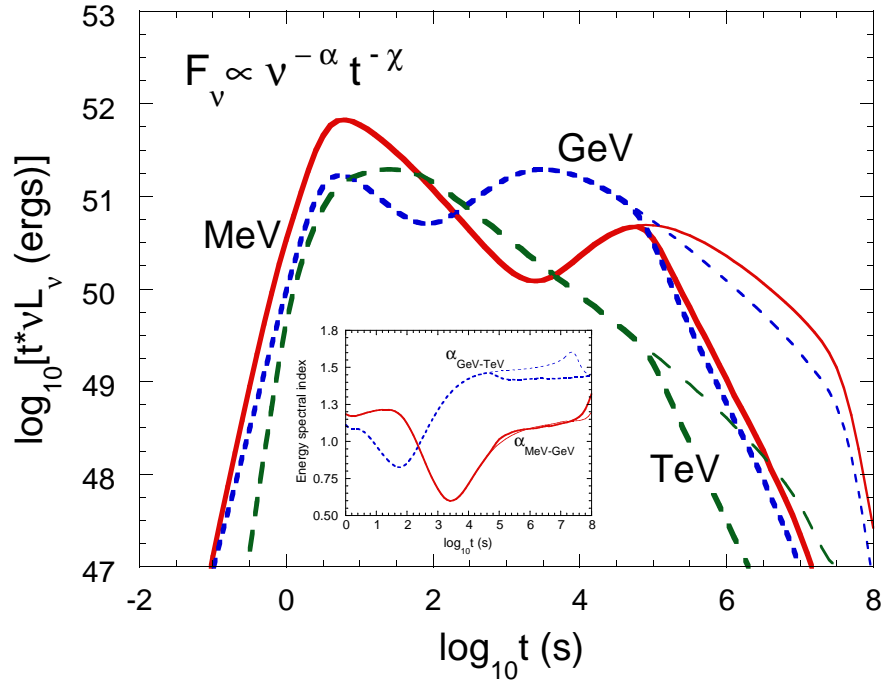


Fig. 5.— Product of  $\nu L_\nu$  flux and observing time  $t$  for the MeV, GeV, and TeV light curves using the  $\theta = 0^\circ$  case in Fig. 2b. Inset shows temporal variation of the broadband MeV–GeV and GeV–TeV energy spectral indices.

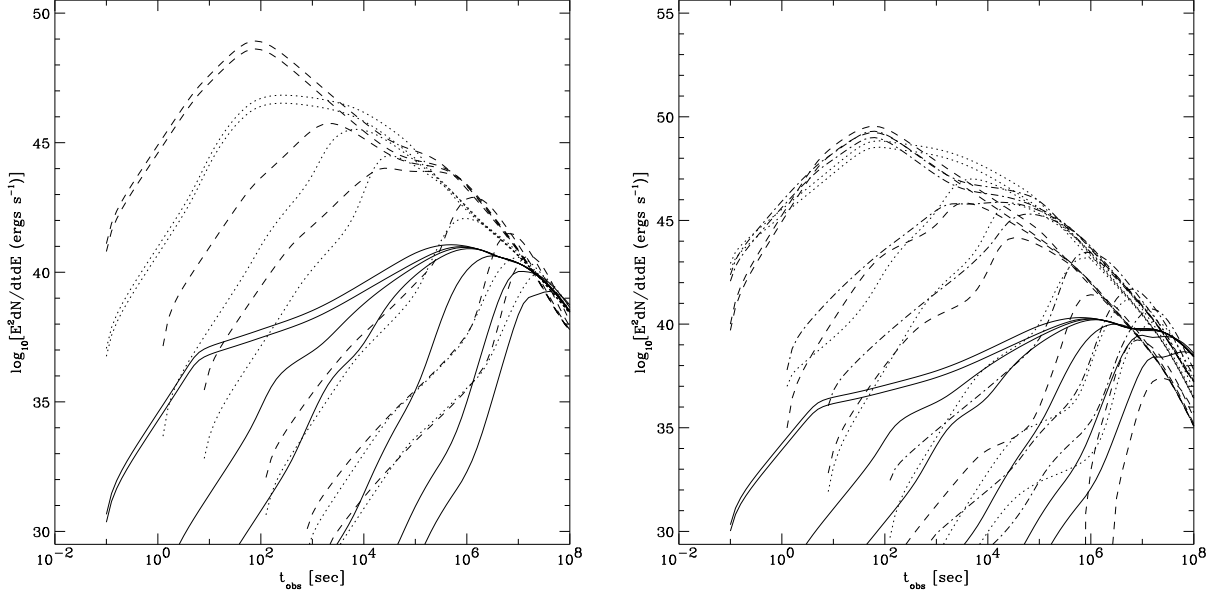


Fig. 6.— Same as Fig. 2, but for an initial blast wave Lorentz factor  $\Gamma_0 = 100$ .

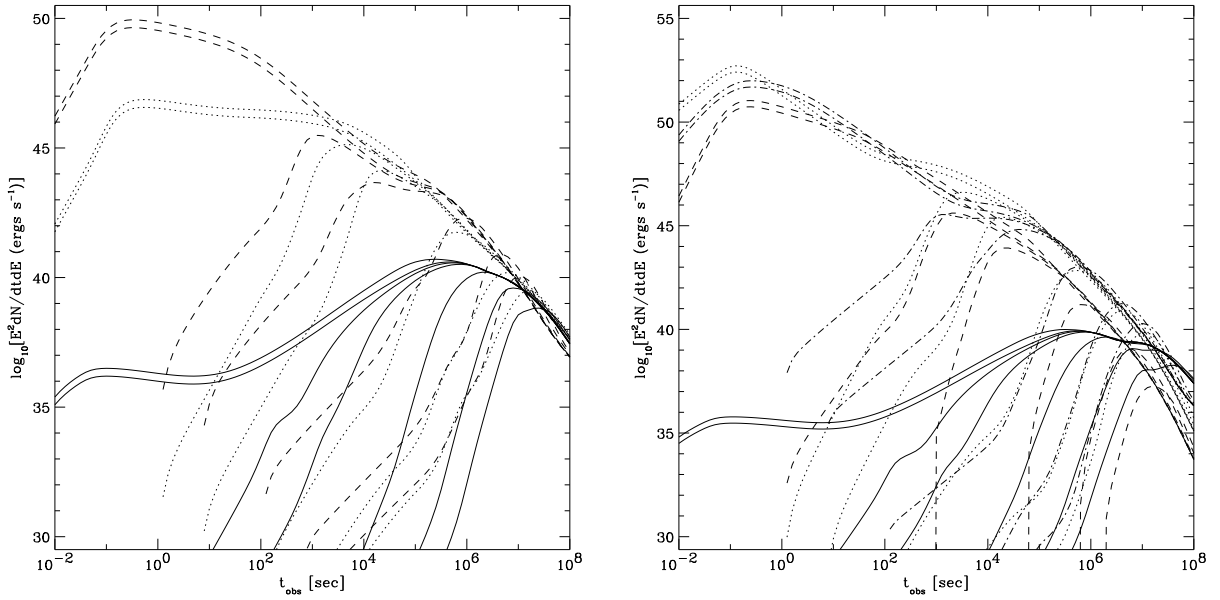


Fig. 7.— Same as Fig. 2, but for an initial blast wave Lorentz factor  $\Gamma_0 = 1000$ .

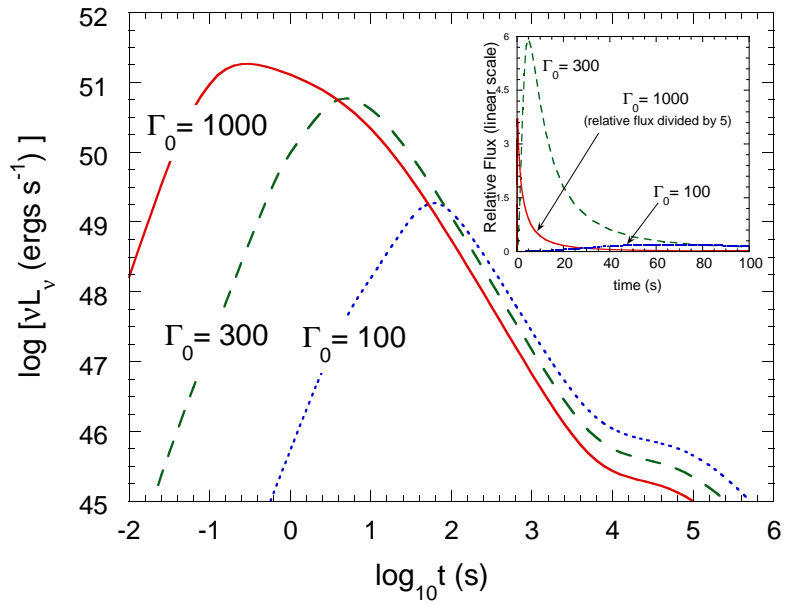


Fig. 8.— Prompt and early afterglow 100 keV light curves for blast wave Lorentz factors  $\Gamma_0 = 1000$  (solid curve), 300 (dashed), and 100 (dotted). Inset shows light curves on a linear scale.